water

MDPI

Article

Degradation of Methylene Blue in the Photo-Fenton-Like Process with WO_3-Loaded Porous Carbon Nitride Nanosheet Catalyst

Weifan Gao [1], Guichang Zhang [1], Xiaoping Zhang [1,2,3,4,*], Shaoqi Zhou [1,2,3,4] and Zihao Wang [1]

1 Guangzhou Higher Education Mega Centre, School of Environment & Energy, South China University of Technology, Guangzhou 510006, China
2 The Key Laboratory of Pollution Control and Ecosystem Restoration in Industry Clusters of Ministry of Education, Guangzhou 510006, China
3 Guangdong Provincial Key Laboratory of Solid Wastes Pollution Control and Recycling, Guangzhou 510006, China
4 Guangdong Provincial Engineering and Technology Research Center for Environmental Risk Prevention and Emergency Disposal, Guangzhou 510006, China
* Correspondence: xpzhang@scut.edu.cn; Tel.: +86-13678920429

Abstract: The catalytic capability of original carbon nitride (CN) is limited by a small specific surface area and high electron–hole recombination rate. In this study, WO_3-loaded porous carbon nanosheets (MCA-CN/WO_3) were synthesized by thermal treatment with melamine, cyanuric acid and WCl_6. The MCA-CN/WO_3 could degrade 98% of the methylene blue (MB) within 30 min in the photo-Fenton-like process, displaying better catalytic activity than the original CN (30%), pure MCA-CN (63%) and original CN/WO_3 (87%). The results of photoluminescence and electrochemical impedance spectroscopy demonstrated that the Z-scheme heterojunction of MCA-CN/WO_3 inhibited the recombination of electrons and holes. In addition, the porous nanosheet structure accelerated the electron transfer and provided abundant active sites for MB degradation. A radical quenching experiment indicated that the Z-scheme heterojunction facilitated the decomposition of H_2O_2 to produce $^1O_2$ for MB degradation. The possible degradation pathways of MB were proposed.

Keywords: photo-Fenton-like process; WO_3-loaded porous carbon nitride nanosheet; Z-scheme heterojunction; MB degradation

Citation: Gao, W.; Zhang, G.; Zhang, X.; Zhou, S.; Wang, Z. Degradation of Methylene Blue in the Photo-Fenton-Like Process with WO_3-Loaded Porous Carbon Nitride Nanosheet Catalyst. *Water* **2022**, *14*, 2569. https://doi.org/10.3390/w14162569

Academic Editor: Sergi Garcia-Segura

Received: 24 July 2022
Accepted: 17 August 2022
Published: 20 August 2022

1. Introduction

Dye wastewater is difficult to deal with due to its characteristics of high chroma and high organic content. Advanced oxidation processes (AOPs) such as photocatalysis, Fenton process, photocatalysis, ozonation, etc., have been extensively used in the actual dye wastewater treatment for their high efficiency, simplicity and no secondary pollution [1,2]. AOPs degrade pollutants into CO_2 and H_2O by active substances such as hydroxyl radical (•OH), superoxide radical ($O_2^{\bullet-}$), sulfate radical ($\bullet SO_4^-$) and singlet oxygen ($^1O_2$). As one of the AOPs, the Fenton process degrades organic pollutants with •OH generated from hydrogen peroxide (H_2O_2) activation in the Fe^{2+}/Fe^{3+} homogeneous system [3]. However, the disadvantages such as narrow pH range, incomplete H_2O_2 decomposition and formation of numerous iron mud limit the widespread application of the technology [4]. To solve these issues, Fenton-like processes are explored, including fabricating heterogeneous catalysts to substitute for Fe^{2+}/Fe^{3+}, as well as combining Fenton processes with photocatalysis and electrochemical oxidation. It is found that the photo-Fenton-like process can accelerate the reaction rate and broaden the pH range through the synergy of light and H_2O_2. Therefore, it is a promising alternative to the traditional Fenton method.

The key to improving the catalytic rate of photo-Fenton-like processes is to prepare a catalyst with good performance. Carbon nitride (CN) is a conjugated polymer semiconductor with a narrow band gap (about 2.7 eV), which has the characteristics of visible light catalytic performance, harmlessness and good stability [5]. Meanwhile, the intrinsic functional groups and vacancies, as well as the sp^2 hybridized configuration of CN, accelerate the generation of electrons [6]. Therefore, CN has developed as a promising material in the Fenton-like process. However, the catalytic capability of original carbon nitride is limited by a small specific surface area and high electron–hole recombination rate [7,8]. Porous carbon nitride nanosheets have a high specific surface area compared to the original bulk carbon nitride, providing more active sites for degradation reactions. In addition, the lamellar structure of CN is beneficial for the electron transfer. Xu et al. synthesized highly porous CN with melamine and cyanuric acid by thermal polycondensation, which exhibited enhanced visible light response and higher electron–hole separation efficiency [9]. Hossein et al. prepared porous CN nanosheets with excellent photodegradation efficiency for Rhodamine B and tetracycline [10]. Based on the above research, fabrication of carbon nanosheets using melamine and cyanuric acid can effectively improve the catalytic performance of CN.

The electron–hole separation efficiency of carbon nitride can be further enhanced by constructing heterojunctions with a metal oxide semiconductor. WO_3 is a nonpoisonous, stable semiconductor photocatalyst with a narrow bandgap (2.7–2.8 eV) and displays high visible light utilization [11]. WO_3 exhibits excellent oxidation capacity due to its positive VB edge potential (+ 3.0 V vs. NHE) [12]. The Z-scheme heterojunction between CN and WO_3 can effectively facilitate the separation of electrons and holes, as well as maintain a high redox capacity [13]. Bai et al. used WO_3/g-C_3N_4 to degrade ciprofloxacin in a photo-electro-Fenton-like system, which revealed enhanced catalytic performance. The results showed that the W^{6+}/W^{5+} cycle promoted the decomposition of H_2O_2, and broadened the pH range without iron sludge [14]. Therefore, WO_3 is a good catalyst in photo-Fenton-like processes for the decomposition of H_2O_2 to form an active substance.

In this paper, the modified carbon nitride (MCA-CN) was synthesized by melamine and cyanic acid through thermal treatment. An appropriate amount of WO_3 was loaded on the MCA-CN to synthesize MCA-CN/WO_3 by thermal treatment. The MCA-CN/WO_3 was used to degrade methylene blue (MB) through the photo-Fenton-like process. Compared with original CN, the MCA-CN/WO_3 displayed enlarged specific surface area and accelerated electron–hole separation. As a consequence, the MCA-CN/WO_3 exhibited superior catalytic performance to original CN for MB degradation in a wide pH range. Combined with the free-radical quenching experiment and EPR analysis, the mechanism of the photo-Fenton catalytic processes was proposed. The intermediate products of MB degradation were determined by LC-MS and possible degradation pathways were put forward. The study provides a reference for CN treatment of MB in the photo-Fenton-like process.

2. Materials and Methods

2.1. Chemicals

All chemicals were reagent grade and used as received. Melamine (ME), cyanuric acid (CA), dimethyl sulfoxide (DMSO), tungsten chloride (WCl_6), sodium hydroxide (NaOH), p-benzoquinone (BQ), 5,5-dimethyl-1-pyrroline-N-oxide (DMPO), ethylene diamine tetra acetic acid disodium (EDTA-2Na), L-histidine (L-His), 4-hydroxy-2, 2, 6, 6-tetramethylpiperidine (TEMP) and methylene blue (MB, $C_{16}H_{20}ClN_3OS$) were supplied by Aladdin Ltd. Hydrogen peroxide (H_2O_2, 30 wt%), isopropyl alcohol (IPA), hydrochloric acid (HCl) and ethanol were obtained from Guangzhou chemical reagent factory. Aqueous solutions were prepared with pure water.

2.2. Synthesis of MCA-CN/WO_3

Typically, 5 g melamine and 5.1 g cyanic acid were dissolved in 200 mL and 100 mL DMSO, respectively, and stirred at 25 °C for 20 min to obtain white precipitation. Then, the precipitation was centrifuged, washed and dried at 50 °C for 12 h. The dried white solid was calcined at 550 °C under a flowing N_2 atmosphere for 4 h [15]. The obtained yellow sample was named MCA-CN.

The MCA-CN/WO_3 catalysts were fabricated by the following steps. Typically, 250 mg MCA-CN and a certain amount of WCl_6 were ground with a small amount of ethanol until the materials turned blue. The blue materials were calcined at a certain temperature in N_2 atmosphere for 1 h to construct a heterojunction (heating rate of 7 °C·min^{-1}) [16]. To optimize the WO_3 content, MCA-CN/WO_3 samples with various WO_3 contents (5 wt%, 15 wt%, 25 wt% and 35 wt%) were prepared. Samples 300 °C MCA-CN/WO_3, 350 °C MCA-CN/WO_3, 400 °C MCA-CN/WO_3 and 450 °C MCA-CN/WO_3 were obtained when the thermal treatment temperatures were 300 °C, 350 °C, 400 °C and 450 °C, respectively. For comparison, pure WO_3 was synthesized without MCA-CN in the same way, and single MCA-CN was second calcined at 350 °C for 1 h without WCl_6. The typical synthetic procedure is shown in Figure 1.

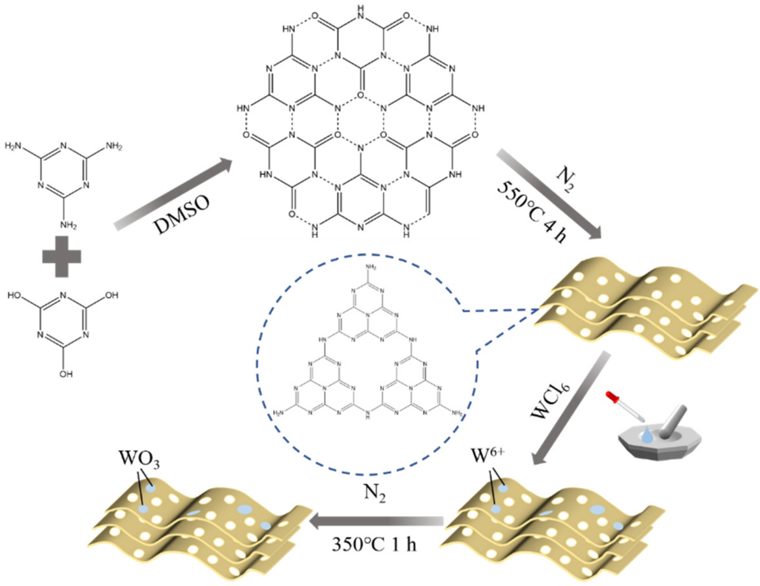

Figure 1. The typical synthetic procedure of MCA-CN/WO_3**.**

2.3. Characterizations

The crystal structure was characterized by X-ray polycrystalline diffraction (XRD, Ultima VI, Akishima-shi, Japan). The geometrical morphology, geometrical size, dispersion state and microelement composition of the material were obtained through scanning electron microscopy (SEM, Merlin Zeiss, Oberkochen, Germany). The morphology, distribution and phase structure of the samples were obtained by 120 kV high-resolution transmission electron microscope (HRTEM, Talos L120c Thermo Fisher, Waltham, MA, USA). Fourier transform infrared spectroscopy (FTIR, infrared thermerfeld IN10, Thermo Fisher Scientific, Waltham, MA, USA) was used to identify the functional groups present in the molecule. The chemical composition and valence band conduction values were obtained by X-ray photoelectron spectroscopy (XPS, Thermo Scientific K-Alpha, Waltham, MA, USA). The pore structure and pore size distribution were characterized by nitrogen adsorption–desorption measurement (Micromeritics APSP 2460, USA). The light absorption range and band gap were obtained by ultraviolet–visible diffuse reflectance absorption spectra (UV DRS, Shimadzu 3600plus, Kyoto, Japan). The charge separation efficiency was detected by photoluminescence spectra (PL, Edinburgh FS5, Livingston, UK) with the excitation wavelength of 380 nm, and $^1O_2$ was measured by electron paramagnetic resonance spectrometer (EPR, ELEXSYS-II E500 CW-EPR, Billerica, Germany). The intermediate products of MB degradation were determined by liquid chromatography–tandem mass spectrometry (LC-MS, Ultimate 3000 UHPLC–Q Exactive, Waltham, MA, USA).

2.4. Photocatalytic Test

A typical experimental suspension contained 0.15 g L^{-1} MCA-CN/WO_3, 0.5 mL H_2O_2 and 20 mg L^{-1} MB (100 mL) at pH 7.4 ± 0.1 in a beaker with constant mechanical stirring at 298 ± 2 K. Before analysis, the MB aqueous solution was stirred in darkness for 30 min to achieve adsorption–desorption equilibrium. Next, the degradation reaction was initiated by adding H_2O_2 and illumination with a 25 W LED lamp ($\lambda > 400$ nm). Water samples were taken every five minutes and filtered by a 0.45 μm membrane. The pH value of MB was adjusted by the HCl solution (1 mol L^{-1}) and NaOH solution (2 mol L^{-1}). The concentration of MB was measured by UV-vis spectrophotometer at the absorption wavelength of 665 nm. The degradation of MB was calculated based on Equation (1) as follows:

$$D = [(C_0 - C)/C_0] \times 100\% \quad (1)$$

where C_0 is the initial concentration of MB at $t = 0$ and C is the instant concentration at photocatalytic degradation time t (min). Moreover, the kinetics reaction constant (k) is obtained by a pseudo-first-order kinetics model as follows (Equation (2)):

$$\ln(C/C_0) = -kt \quad (2)$$

2.5. Photoelectrochemical Measurement

Photoelectrochemical measurement was carried out on a CHI 660E electrochemical workstation with a three-electrode system. Ag/AgCl electrode and Pt wire were used as reference and counter electrodes, respectively. For the preparation of the working electrode, 10 mg of the sample was mixed with 1 mL ethanol and 80 μL Nafion solution under ultrasonication for 30 min. Then, 40 μL of the suspension was coated on Fluorine-doped Tin Oxide (FTO) glass, and dried at room temperature. Electrochemical impedance spectroscopy (EIS) measurement was measured in a 0.5 M Na_2SO_4 solution in the frequency range of 0.01 Hz to 100 kHz under the irradiation of 300 W Xe lamps.

2.6. Radical Quenching Experiments

The reactive oxygen species (ROS) including ·OH, h^+,$\cdot O_2^-$ and $^1O_2$ were captured by adding a certain amount of isopropyl alcohol (IPA), ethylenediamine tetra acetic acid disodium (EDTA-2Na), p-benzoquinone (BQ) and L-histidine (L-His), respectively. Singlet oxygen ($^1O_2$) was detected in water with 2,2,6,6-tetramethylpiperidine (TEMP) by electron paramagnetic resonance (EPR).

3. Results

3.1. Characterization

The SEM images (Figure 2a) showed that the original carbon nitride is lumpy with no obvious pores, while MCA-CN displayed crimped porous carbon nanosheet morphology (Figure 2b). This result indicated that the morphological regulation of carbon nitride by cyanuric acid can make the carbon nitride into loose porous nanosheets, providing more active sites for MB degradation. The lamellar structure ensures strong interaction of carbon nitride and WO_3, accelerating the electron transfer between carbon nitride and WO_3. Figure 2c showed the SEM image of MCA-CN/WO_3, and it can be seen that the structure of MCA-CN was destroyed because of the load of WO_3. As shown in the TEM images (Figure 2d), MCA-CN/WO_3 exhibited the shape of folded nanosheets. Figure 2e showed the layered structure of MCA-CN/WO_3, with the lighter region being MCA-CN and the region with the lattice stripe being WO_3. As shown in the HRTEM image (Figure 2f), the lattice fringes of 0.383 nm corresponded to the (002) crystal plane of WO_3 [14]. The survey spectrum of MCA-CN/WO_3 (Figure 2g) showed the element of carbon and nitrogen accounted for a relatively high proportion. EDX analysis (Figure 2h–k) showed that carbon, nitrogen, oxygen and tungsten elements distributed uniformly in the catalyst, indicating the successful synthesis of MCA-CN/WO_3 [17].

The phase composition of materials was investigated by XRD. As displayed in Figure 3a, MCA-CN showed two characteristic peaks at 27.5° and 12.8°, corresponding to interplanar aromatic stacking (002) and intraplanar stacking (100) of carbon nitride [18]. For MCA-CN/WO_3, the new diffraction peaks at 23.5° corresponded to the standard card PDF#83-0949 of WO_3, indicating the successful coupling of WO_3 and MCA-CN. In addition, the broad peak of WO_3 showed amorphous features. Other characteristic diffraction peaks of WO_3 were not observed because of its weak crystallization and low loading content. To further determine the generation of WO_3, the XRD pattern of pure WO_3 was conducted. Obviously, the diffraction peaks of WO_3 were consistent with the standard card PDF#83-0949, demonstrating the successful generation of WO_3.

FT-IR spectra of WO_3, MCA-CN and MCA-CN/WO_3 are shown in Figure 3b. For pure MCA-CN, the broad absorption vibration peak at 2900–3500 cm^{-1} corresponded to the band of N−H or O−H [19]. The absorption band ranging from 1200 to 1600 cm^{-1} belonged to the stretch of C−N and C=N in CN heterocycles [20]. The strong absorption vibration peak at 810 cm^{-1} was related to the characteristic vibration of the triazine ring unit [21]. For pure WO_3, the wide absorption peak at 500–1000 cm^{-1} corresponded to the vibration of the O−W−O bond [22]. For the MCA-CN/WO_3 composites, the absorption peaks at 1200–1600 cm^{-1} were similar to those of MCA-CN, indicating that the structure of MCA-CN was not changed by WO_3. The typical absorption peak of WO_3 at 500–1000 cm^{-1} was also observed in the spectrum of MCA-CN/WO_3, further proving the successful heterojunction construction of MCA-CN and WO_3 [23].

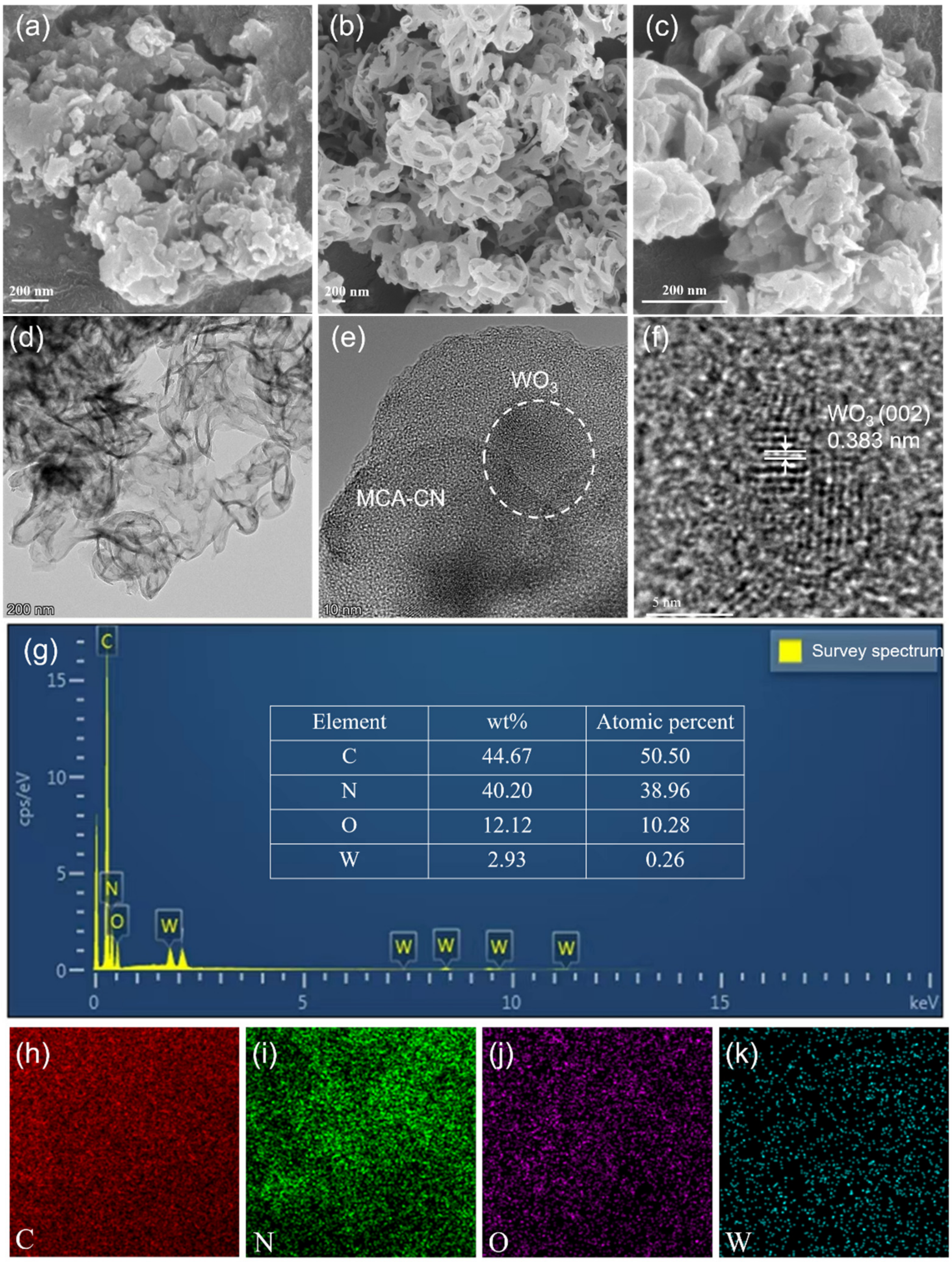

Figure 2. SEM images of (**a**) bulk CN; (**b**) MCA-CN and (**c**) MCA-CN/WO_3. (**d**–**f**) TEM images of MCA-CN/WO_3; (**g**) survey spectrum of MCA-CN/WO_3 and (**h**–**k**) EDX spectrum and elemental mapping images of MCA-CN/WO_3.

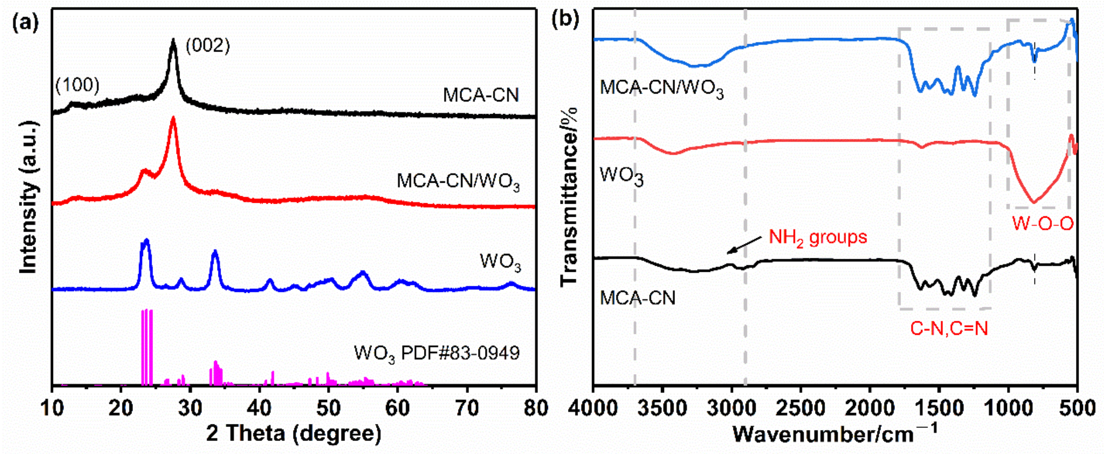

Figure 3. (**a**) XRD patterns of MCA-CN and MCA-CN/WO_3 and (**b**) FTIR patterns of MCA-CN, WO_3 and MCA-CN/WO_3.

The elemental composition and surface chemical states of MCA-CN/WO_3 were revealed by XPS. The signals of C, N, O and W elements were observed in the full scan spectrum of MCA-CN/WO_3 (Figure 4a). For the C1s spectrum shown in Figure 4b, the four characteristic peaks at 284.6 eV, 286.5 eV, 288.2 eV and 289.2 eV corresponded to C–C, C–N–C, N–C=N and O–C=O, respectively [24]. The three characteristic peaks of 398.5 eV, 399.5 eV and 401.1 eV in the N1s spectra corresponded to the sp^2 nitrogen N–C=N, N–(C)3 and C–N–H on the triazine ring, respectively (Figure 4c) [25]. As shown in Figure 4d, the O1s spectrum displayed three peaks at 530.6 eV, 532.0 eV and 533.2 eV. The peak at 530.6 eV corresponded to W–O–W in WO_3 [26]. The peak at 532.0 eV was ascribed to the existence of the OH group, which can capture photogenerated holes and inhibit the recombination of electron and hole [27]. The peak at 533.2 eV was related to H_2O or CO_2 adsorbed from the air. Figure 4e presents the spectrum of W 4f. The peaks at 37.13 eV and 35.07 eV corresponded to W $4f_{5/2}$ and W $4f_{7/2}$ of W^{6+}, respectively [11]. Two peaks at 35.8 eV and 33.8 eV were ascribed to W $4f_{7/2}$ and W $4f_{5/2}$ of W^{5+} [28].

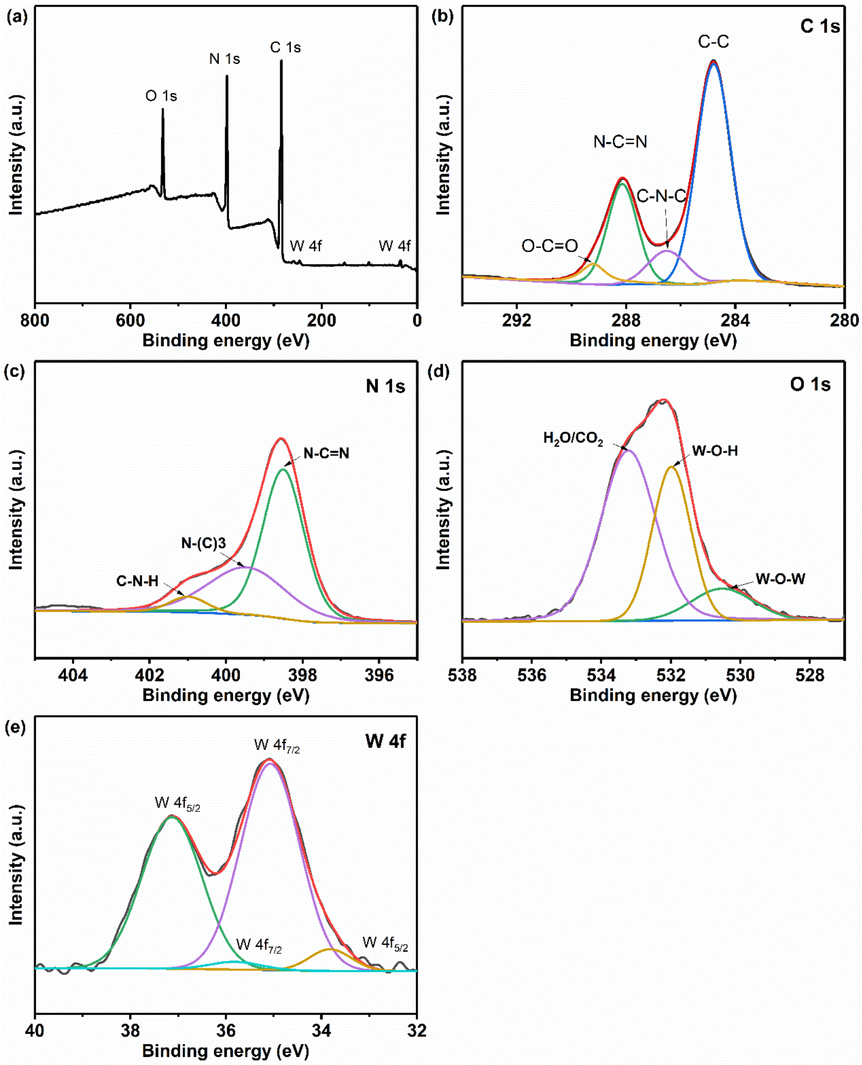

Figure 4. XPS spectra of MCA-CN/WO_3. (**a**) Survey spectrum. (**b**) C1s and (**c**) N1s spectra of MCA-CN/WO_3. (**d**) O1s and (**e**) W 4f spectra of MCA-CN/WO_3.

The N_2 adsorption–desorption isotherms and the Barrett–Joyner–Halenda (BJH) pore size distribution curves of ME-CN, MCA-CN and MCA-CN/WO_3 are displayed in Figure 5. In N_2 adsorption–desorption isotherms, all samples showed type IV isotherms with a type H3 hysteresis loop, indicating the presence of mesoporous structures (Figure 5a). As shown in BJH pore size distribution curves (Figure 5b), all samples exhibited a wide range distribution of pore size. There were two peaks at 2.75 nm and 27.8 nm in in the curve of MCA-CN, indicating that the pore size distributed from 2 nm to 30 nm. The BET specific surface area, pore volume and pore size of the materials were calculated by the BJH method and are listed in Table 1. The BET specific surface areas of ME-CN, MCA-CN and MCA-CN/WO_3 composites were calculated to be 10.4, 74.4 and 53.8 $m^2\ g^{-1}$. The specific surface area of MCA-CN is 7.1 times higher than that of ME-CN. Obviously, the increased surface area and mesopores of carbon nitride are attributed to the addition of cyanic acid, providing more active sites for catalytic degradation of pollutants. In addition, the porous structure also contributes to enhanced light absorption, since light is reflected multiple times within the holes. However, MCA-CN/WO_3 had a lower surface area than MCA-CN, because WO_3 is coarse and lumpy with a small specific surface area, and the load of WO_3 covered part of the pores of MCA-CN.

Table 1. Surface area, pore volume and pore size of ME-CN, MCA-CN and MCA-CN/WO_3.

Samples	Surface Area (m^2 g^{-1})	Pore Volume (cm^3 g^{-1})	Pore Size (nm)
ME-CN	10.43	0.025	28.66
MCA-CN	74.44	0.168	24.36
MCA-CN/WO_3	53.84	0.135	27.50

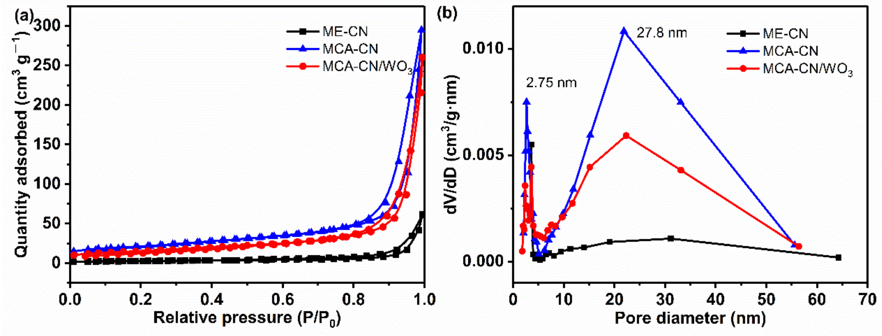

Figure 5. (**a**) N_2 adsorption/desorption isotherm of ME-CN, MCA-CN and MCA-CN/WO_3 and (**b**) pore size distribution curves of ME-CN, MCA-CN and MCA-CN/WO_3.

3.2. Photochemical Characterization

The optical performance of the ME-CN, MCA-CN, WO_3 and MCA-CN/WO_3 catalysts were studied by UV-vis DRS. As displayed in Figure 6a, pure MCA-CN exhibited an absorption edge at about 470 nm. Compared with ME-CN (461 nm), the absorption edge of MCA-CN moved to the visible region. This is because the abundant mesopores of MCA-CN can absorb more light radiation. Compared with pure MCA-CN, there was a red shift (490 nm) and significantly enhanced light absorption capacity of MCA-CN/WO_3, which ascribed to the heterojunction between MCA-CN and WO_3. Based on the Kubelka–Munk function (Equation (3)), the band gaps (E_g) of ME-CN, MCA-CN and MCA-CN/WO_3 were determined to be 2.62, 2.54 eV and 2.41 eV, as depicted in Figure 6b. Figure 6c shows that the E_g of WO_3 was 2.50 eV. Obviously, the band gap of carbon nitride was effectively reduced by modification of cyanic acid and WO_3. The reduction in the band gap made it easier for MCA-CN/WO_3 to form photogenerated carriers, promoting the separation of electrons and holes.

$$\alpha h\upsilon^{(1/n)} = A(h\upsilon - E_g) \tag{3}$$

where α, h, ν and A represent the adsorption coefficient, Planck's constant, light frequency and a constant, respectively. The value of n is determined by the type of semiconductor (1/2 for the indirect band gap and 2 for the direct band gap). Herein, the values of n for MCA-CN and WO_3 were 2 and 1/2, respectively.

Moreover, the valance band (E_{VB}) and conduction band (E_{CB}) of MCA-CN and WO_3 could be calculated via the following formulas [29]:

$$E_{VB} = X - E_e + 0.5E_g \tag{4}$$

$$E_{CB} = E_{VB} - E_g \tag{5}$$

where X is the absolute electronegativity of the catalyst (X-MCA-CN = 4.72 eV and X-WO_3 = 6.58 eV) and E_e is the energy of free electrons vs. hydrogen (4.5 eV). According to the above Equations (4) and (5), the E_{VB}, E_{CB} of ME-CN, MCA-CN and WO_3 are calculated and listed in Table 2. Obviously, there was an alternating band structure between MCA-CN and WO_3, efficiently improving the photogenerated charge separation and degradation rate of pollutants.

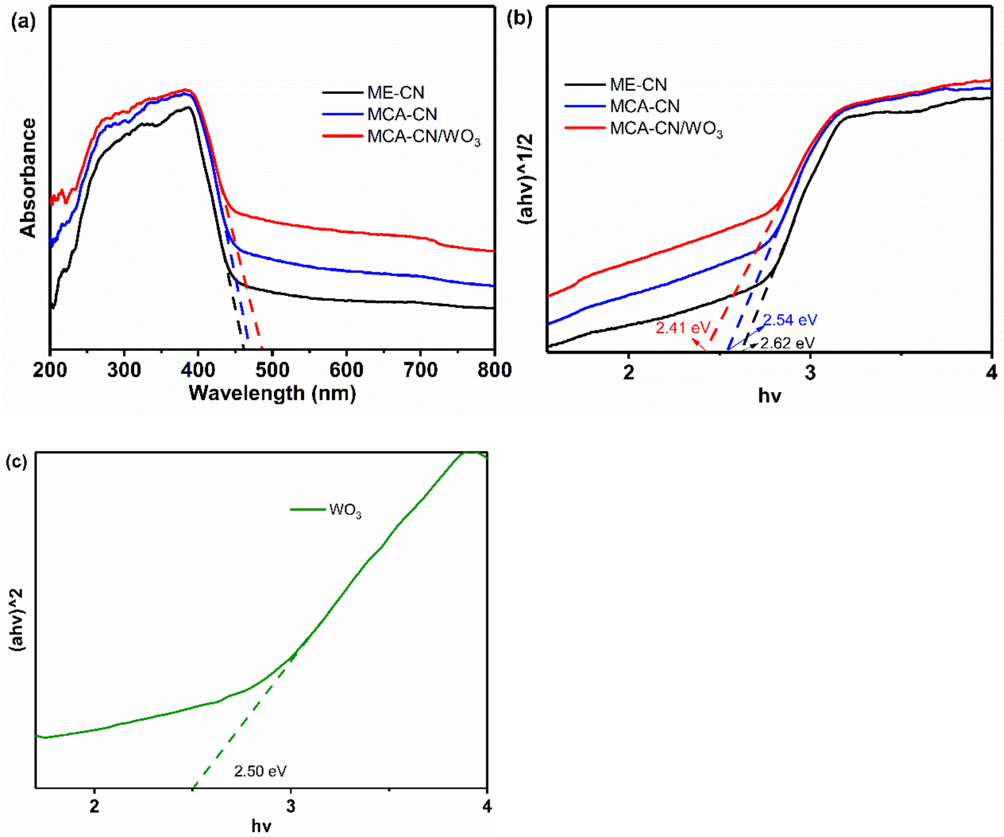

Figure 6. (**a**) DRS of MCA-CN/WO3, ME-CN/WO3 and MCA-CN/WO3; (**b**) corresponding plots of the transformed Kubelka–Munk function; (**c**) plots of the transformed Kubelka–Munk function.

Table 2. Energy Band Potentials of ME-CN, MCA-CN and WO_3.

Samples	E_g (eV)	E_{VB} (eV)	E_{CB} (eV)
ME-CN	2.62	1.53	−1.09
MCA-CN	2.54	1.49	−1.05
WO_3	2.50	3.33	0.83

PL spectroscopy under the excitation at 380 nm and EIS spectra were conducted to measure the electron–hole separation rate of MCA-CN/WO_3. Generally, the weaker the PL intensity, the higher the separation efficiency of catalysts. As shown in Figure 7a, the PL intensity of MCA-CN was weaker than that of ME-CN, implying that MCA-CN exhibited higher electron–hole separation efficiency than ME-CN. Compared with MCA-CN, the significant decrease in PL intensity of MCN indicated the inhibited recombination of electron and hole. EIS spectra are depicted in Figure 7b. The diameter of ME-CN, MCA-CN and MCA-CN/WO_3 decreased in sequence, indicating the lowest electron–hole complexation rate of MCA-CN/WO_3. Therefore, the nanosheet structure of MCA-CN and the heterojunction between MCA-CN and WO_3 effectively improved the separation efficiency of electron and hole.

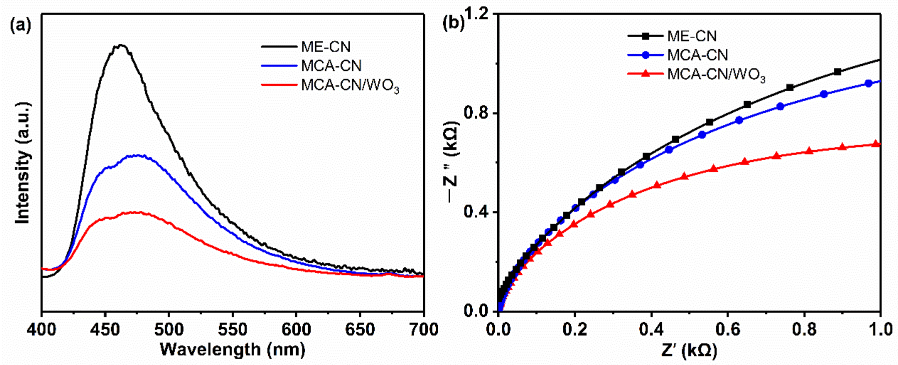

Figure 7. (**a**) PL spectra and (**b**) EIS Nyquist plots of ME-CN, MCA-CN and MCA-CN/WO_3.

3.3. Catalytic Performance

3.3.1. Photo-Fenton Performance of Catalysts

The catalytic activities of MCA-CN/WO_3 composites were examined by degrading MB in the presence of H_2O_2 and visible light. As exhibited in Figure 8a, there was little MB degraded in photo-Fenton system without catalysts, indicating the negligible radical production by H_2O_2 without catalysts. After adding MCA-CN/WO_3 catalysts, the removal rate of MB reached 98% within 30 min. This result suggested that MCA-CN/WO_3 composites were highly efficient catalysts for H_2O_2 activation to produce reactive radicals. The MB degradation efficiency of MCA-CN (63%) was higher than that of ME-CN (30%), which ascribed to the larger specific surface area of MCA-CN. MCA-CN/WO_3 exhibited better catalytic performance than MCA-CN, suggesting that the heterojunction between MCA-CN and WO_3 accelerated the decomposition of H_2O_2 for improving catalytic activity. The MB degradation efficiency of ME-CN/WO_3 (87%) was lower than that of MCA-CN/WO_3, indicating that the sheet-like structure of MCA-CN can enhance catalytic performance. Moreover, in the MCA-CN/WO_3 photo-Fenton-like process, the degradation rate was higher than when H_2O_2 (38%) and light (10%) were present alone. This result indicated that the synergistic effect of catalysts, H_2O_2 and visible light could significantly enhance the removal efficiency of MB. Figure 8b displays the reaction rate constants (k) obtained through the Langmuir–Hinshelwood kinetics model. Among all the materials, the rate constant of MCA-CN/WO_3 (0.1465 min^{-1}) was the highest, which was about 12.4, 4.7 and 2.1 times higher than that of ME-CN (0.0118 min^{-1}), MCA-CN (0.0314 min^{-1}) and ME-CN/WO_3 (0.0685 min^{-1}). Furthermore, the kinetic constant of MCA-CN/WO_3 in the photo-Fenton-like process was 37.5, 9.5 times higher than its rate constant in the corresponding photocatalytic processes (0.0037 min^{-1}) and Fenton-like processes (0.0154 min^{-1}). The photo-Fenton degradation of pollutants over g-C_3N_4-based photocatalysts is shown in Table S1, and MCA-CN/WO_3 displayed better degradation performance than most of those catalysts.

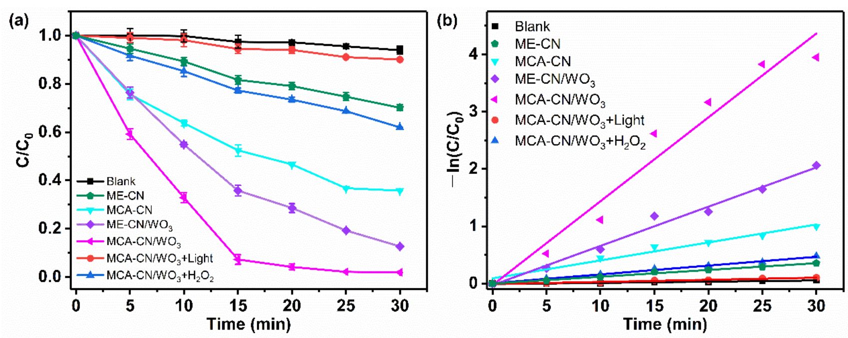

Figure 8. (**a**) Degradation curves of MB under different conditions and (**b**) reaction rate constants associated with MB degradation.

3.3.2. Performance Optimization of MCA-CN/WO_3

To obtain optimized preparation conditions for high-performance MCA-CN/WO_3, two experimental parameters were adjusted, the loading amount of WO_3 and the heat treatment temperature. As exhibited in Figure 9a, the removal rate of MB increased gradually as the WO_3 content increased from 5% to 25%. When the content of WO_3 was 35%, there was little improvement in the degradation efficiency. Excess WO_3 induced interparticle aggregation, thus decreased interfacial contact with MCA-CN and lowered photocatalytic performances. Therefore, the optimal content of WO_3 in the composite was 25%. The degradation properties of catalysts synthesized at temperatures from 300 °C to 450 °C are shown in Figure 9b. Obviously, catalysts synthesized at 300 °C and 350 °C showed better catalytic performance than that at 400 °C and 450 °C. Furthermore, the catalysts synthesized at 300 °C, 350 °C and 450 °C were characterized by XRD (Figure S2). There were no obvious diffraction peaks of WO_3 in the curve of 300 °C MCA-CN/WO_3, indicating that WO_3 cannot be formed at 300 °C, while there were impure peaks in the curve of 450 °C MCA-CN/WO_3, owing to the decomposition of MCA-CN. Hence, 350 °C was the most appropriate temperature to synthesize the sample with good catalytic performance.

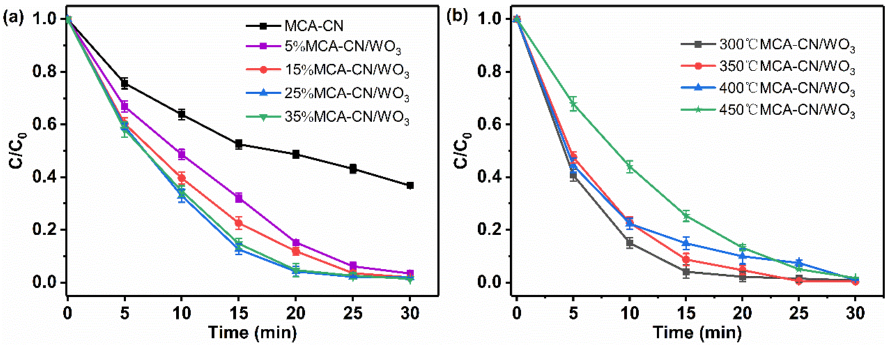

Figure 9. Degradation rate of MB with (**a**) different loading amount of WO_3 and (**b**) different synthesized temperatures.

3.3.3. The Effect of Experimental Parameters

The effects of pH, amounts of H_2O_2 and catalyst (25% MCA-CN/WO_3) on the removal efficiency of MB in the photo-Fenton system were explored to optimize the reaction conditions. It is obvious from Figure 10a that the sample maintained excellent degradation performance in the pH range of 4.3 to 12.3. In addition, the higher the pH value, the better the degradation of MB. About 57% of MB was degraded in 30 min at pH 2.4, but when increasing the pH value to 12.3, the degradation rate reached 99.5% in 30 min. Under acidic conditions, high concentrations of H^+ will scavenge $HO_2\bullet$ ($HO_2\bullet + H^+ + e^- \rightarrow H_2O_2$) [30], while high pH is beneficial to the survival of $HO_2\bullet$ and lowers the redox potential of the conduction band to form more $HO_2\bullet$. Since $^1O_2$ formed via $HO_2\bullet$ was responsible for the removal of MB, there was more $^1O_2$ produced at a higher pH, improving the MB degradation efficiency.

H_2O_2 is the main substance that generates radicals in the Fenton system. As displayed in Figure 10b, the MB degradation efficiency increased from 95% to 99% in 30 min with an increase in the amount of H_2O_2 from 0.1 to 0.5 mL. The degradation rate of MB improved slightly with the addition of 0.9 mL H_2O_2. When the amount of H_2O_2 exceeded 0.9 mL, the removal rate decreased with the increase in H_2O_2 content. At high H_2O_2 concentrations, the excess H_2O_2 molecules removed the valuable radical species, resulting in a decrease in efficiency [31]. Considering both degradation effectiveness and cost, the optimum amount of H_2O_2 for the catalytic degradation of MB in the photo-Fenton system was 0.5 mL.

The effect of catalyst amount on the degradation rate is illustrated in Figure 10c. With the catalyst dosage increasing, the degradation rate was faster. However, when the amount of catalyst increased from 0.15 to 0.25 g L^{-1}, there was almost no difference in the degradation rate at 30 min. Generally, increasing the amount of catalyst would enhance the absorption of light and pollutant, thus improving the catalytic activity. However, from the adsorption curve in Figure S1 (Supplementary Materials), it could be concluded that when the catalyst dosage exceeded 0.20 g L^{-1}, the removal of pollutants was mainly attributed to adsorption rather than degradation. Hence, in order to study the degradation of MB by catalyst, the optimum amount of the catalyst was 0.15 g L^{-1}.

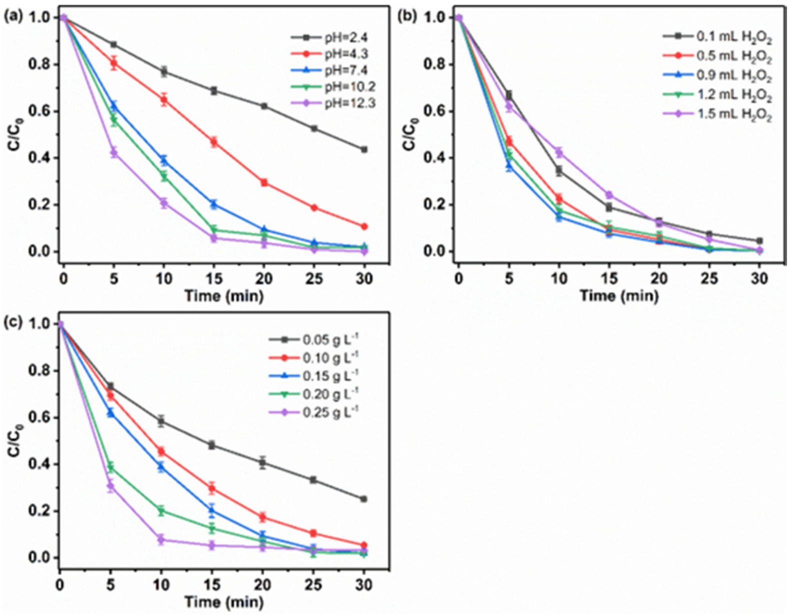

Figure 10. The effect of (**a**) pH, (**b**) amount of H_2O_2 and (**c**) catalyst dosage on degradation of MB in MCA-CN/WO_3/H_2O_2/visible light system.

3.4. Degradation Mechanism

To investigate the mechanism of MB degradation by the MCA-CN/WO_3 composite, a quenching experiment and EPR analysis were conducted to determine the main active radicals for MB degradation.

In radical quenching tests, IPA, p-BQ, EDTA-2Na and L-His were used to eliminate •OH, $•O_2^-$, h^+ and $^1O_2$, respectively. As exhibited in Figure 11a, the degradation rate of MB decreased slightly when IPA, EDTA-2Na and p-BQ were added into the system. However, the degradation of MB decreased from 98% to 40% within 30 min after the adding of L-His. The results indicated that $^1O_2$ radicals were responsible for MB removal in the photo-Fenton system of the MCA-CN/WO_3 composite, while •OH, $•O_2^-$ and h^+ had a slight effect on MB degradation.

EPR analysis was conducted to confirm the role of $^1O_2$ in the reaction. The $^1O_2$ was captured by TEMP and generated a 1:1:1 triplet signal, as displayed in Figure 11b. In comparison with bare MCA-CN system, the signal produced in the MCA-CN/WO_3 system was much stronger, indicating that more $^1O_2$ was produced in the MCA-CN/WO_3 system. This was consistent with the previous results shown in Figure 11a, demonstrating that $^1O_2$ played a critical role for the removal of MB. Typically, $^1O_2$ can be generated through three pathways: (1) the oxidation of $•O_2^-$ produced by O_2 [32]; (2) The Haber–Weiss reaction between $•O_2^-$/$HO_2•$ and H_2O_2 [33]; (3) the recombination of $•O_2^-$/$HO_2•$ [34]. To explore the origin of $^1O_2$, the degradation rate of MB with MCA-CN/WO_3 in nitrogen atmosphere was tested. As depicted in Figure 11a, the MB degradation remained unchanged in the presence of N_2, indicating that O_2 was not the precursor of $^1O_2$ in this reaction. Therefore, we could speculate that H_2O_2 was the only source for $^1O_2$ generation in the MCA-CN/WO_3

photo-Fenton system. As displayed in radical quenching tests, $\bullet O_2^-$ had little effect on MB degradation. Hence, it was speculated that H_2O_2 was converted into $^1O_2$ via the Haber–Weiss reaction between $HO_2\bullet$ and H_2O_2, or the recombination of $HO_2\bullet$. The reaction rate constant of $HO_2\bullet$ recombination is 8.3×10^5 M^{-1} s^{-1} [35], which is about five magnitudes larger than that of $HO_2\bullet$ and H_2O_2 (3 M^{-1} s^{-1}) [36,37]. Therefore, $HO_2\bullet$ recombination was dominant for $^1O_2$ generation in the photo-Fenton system of the MCA-CN/WO_3 catalyst.

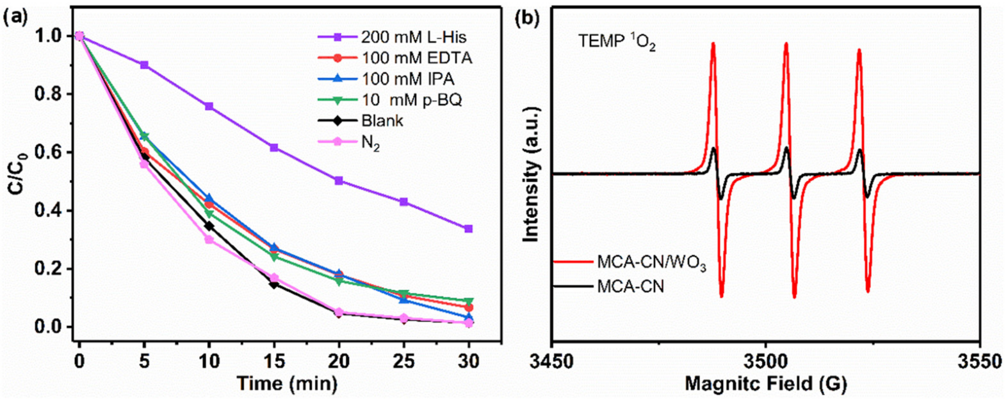

Figure 11. (**a**) Quenching experiment of different radicals and (**b**) EPR spectra for TEMP adducts in photo-Fenton-like system of MCA-CN and MCA-CN/WO_3.

The energy band structures of MCA-CN/WO_3 obtained by UV-Vis DRS are shown in Figure 12. For such an energy band structure, there are usually two possible charge transfer mechanisms: (1) type II heterojunctions and (2) Z-scheme heterojunctions [38]. Supposing there is a type II heterojunction between MCA-CN and WO_3, photogenerated holes are transferred from the VB of WO_3 to the VB of MCA-CN, while photogenerated electrons are transferred from the CB of MCA-CN to the CB of WO_3 with a positive potential (grey dashed line in Figure 12). However, due to the lower reduction potential of $H_2O_2/HO_2\bullet$ (E^0 = 1.65 V. NHE) than the VB potentials of MCA-CN (1.49 eV) [39], the holes on the VB of MCA-CN cannot decompose H_2O_2 into $HO_2\bullet$. This is not consistent with the above conclusion that $^1O_2$ is produced by $HO_2\bullet$. For a Z-scheme heterojunction, the electrons on the CB of WO_3 are transferred to the VB of MCA-CN (solid blue line in Figure 12), and the VB potential of WO_3 (3.12 eV) is lower than $H_2O_2/HO_2\bullet$ (E^0 = 1.65 V. NHE), allowing the production of $HO_2\bullet$. The above analysis suggested that the charge transfer mechanism of MCA-CN/WO_3 was Z-scheme.

A possible photo-Fenton-like catalytic mechanism for MB degradation on the MCA-CN/WO_3 composite was proposed, as illustrated in Figure 12 and the following equations. Under visible light irradiation, both WO_3 and MCA-CN were activated, along with the generation of electron–hole pairs. Electrons from the CB of WO_3 transferred spontaneously to the VB of MCA-CN to recombine with the holes from MCA-CN. Accordingly, most of the electrons were accumulated on the CB of MCA-CN, while the predominated holes were inhabited on the VB of WO_3. In this way, holes and electrons were separated effectively (Equation (6)), which attributed to the Z-scheme heterojunction between WO_3 and MCA-CN nanosheets. In the traditional Fenton system, radicals can be generated through the decomposition of H_2O_2 catalyzed by Fe^{2+}/Fe^{3+} [40]. Similarly, the conversion between W^{6+} and W^{5+} could promote the decomposition of H_2O_2 [16]. W^{6+} gained an electron to form W^{5+}, and W^{5+} decomposed H_2O_2 into $^1O_2$ by the oxidation of h^+ (Equations (7) and (8)). In addition, $HO_2^\bullet$ was produced by the reaction between H_2O_2 and W^{6+} (Equation (9)), subsequently recombined to form $^1O_2$ (Equation (10)). Ultimately, the plentiful active species $^1O_2$ decomposed MB into CO_2, H_2O and degradation intermediates (Equation (11)) [41,42].

$$\text{MCA-CN/WO}_3 + h\nu \rightarrow h^+ + e^- \quad (6)$$

$$W^{6+} + e^{-} \rightarrow W^{5+} \quad (7)$$

$$2H_2O_2 + W^{5+} + h^{+} \rightarrow W^{6+} + 2H_2O + {}^1O_2 \quad (8)$$

$$H_2O_2 + W^{6+} \rightarrow W^{5+} + HO_2^{\bullet} + H^{+} \quad (9)$$

$$HO_2^{\bullet} + HO_2^{\bullet} \rightarrow H_2O_2 + {}^1O_2 \quad (10)$$

$$MB + {}^1O_2 \rightarrow CO_2 + H_2O \quad (11)$$

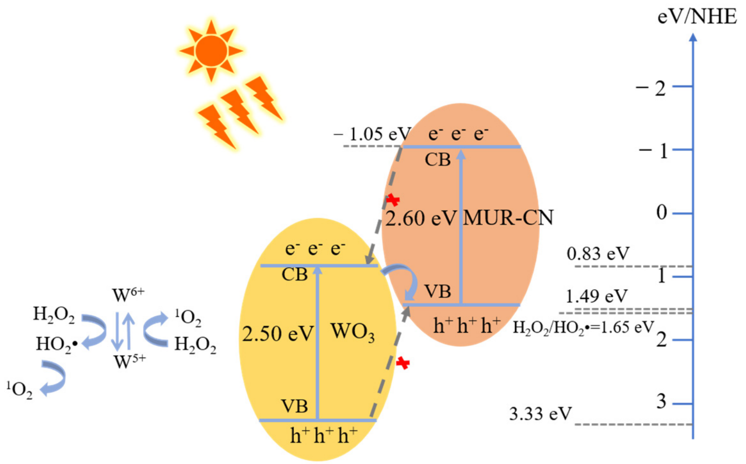

Figure 12. Schematic illustration of catalytic mechanism of MCA-CN/WO_3 in photo-Fenton-like process.

To investigate the degradation pathways of MB in the photo-Fenton-like process, the intermediate products at 30 min of the reaction were determined using LC-MS. The structures of the intermediates were obtained through the Nist standard database and are listed in Table S2 (Supplementary Materials) and Figure S3 (Supplementary Materials), showing the mass spectrum of intermediates. Degradation pathways are shown in Figure 13. Among the molecules of MB, the C-S molecular bond has the smallest bond energy and is easy to break. The N of the C-N bond is also susceptible to be oxidated because of its low electronegativity. Under the attack of ${}^1O_2$, the bond between the methyl group and C was cracked. In pathway 1, the MB was changed into intermediate A when S was oxidized to S=O. The intermediate A was transformed to intermediate B when the C-N bonds broke. Then, the C-S bond broke and intermediate B was transformed to intermediate C. In pathway 2, the MB was changed into intermediate D owing to the cracking of C-S bonds. With the strong oxidation capacity of ${}^1O_2$ and •OH, intermediate D is oxidized to form intermediate E. As the reaction continued, intermediate C and intermediate E would decompose into small molecule organic acids, SO_4^{2-}, NO_3^{-}, CO_2 and H_2O.

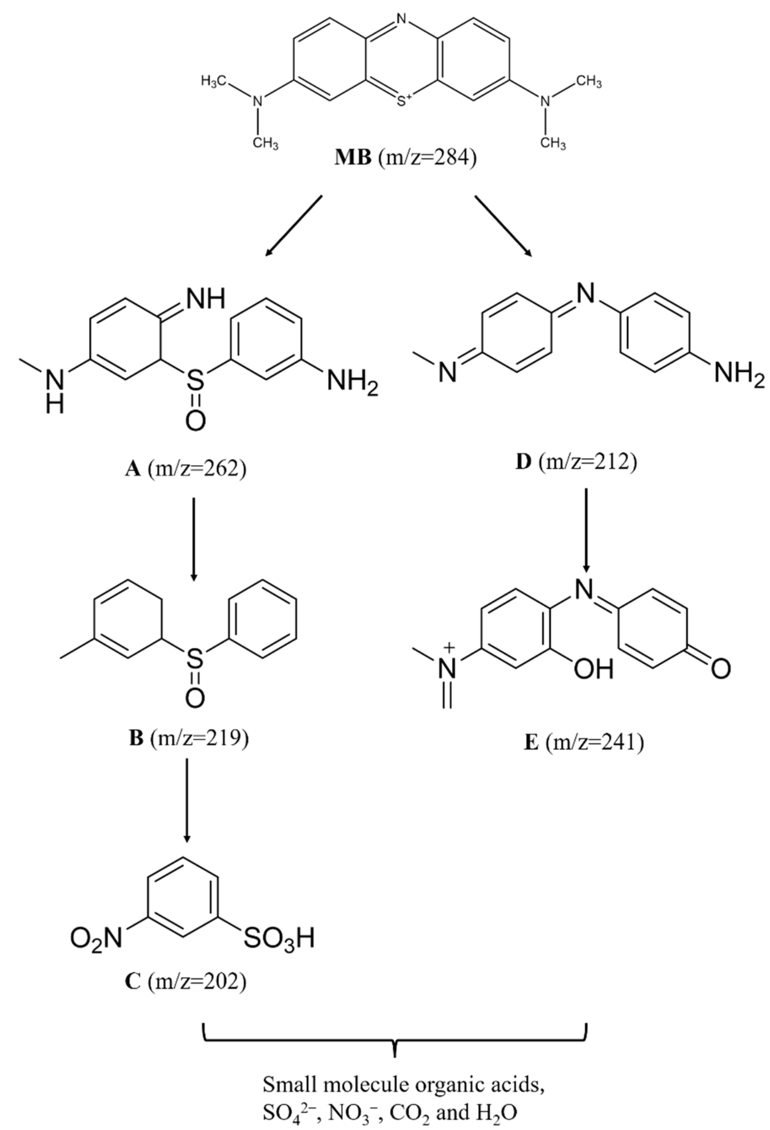

Figure 13. Possible pathways of MB degradation in MCA-CN/WO_3/H_2O_2/visible light system.

3.5. Stability of MCA-CN/WO_3 Catalyst

The stability of a catalyst is one of the most important indexes of its practicability. A cycling experiment was conducted to evaluate the reusability of MCA-CN/WO_3. As shown in Figure 14a, even after five cycles, the MCA-CN/WO_3 catalyst exhibited high catalytic performance, degrading 85% of the MB in 30 min. The XRD spectra of the five cycles of MCA-CN/WO_3 used were carried out (Figure 14b). Compared with the XRD patterns of the fresh MCA-CN/WO_3 catalyst, the diffraction peak of MCA-CN/WO_3 after five cycles did not change greatly, indicating the good stability and reusability of the MCA-CN/WO_3 catalyst.

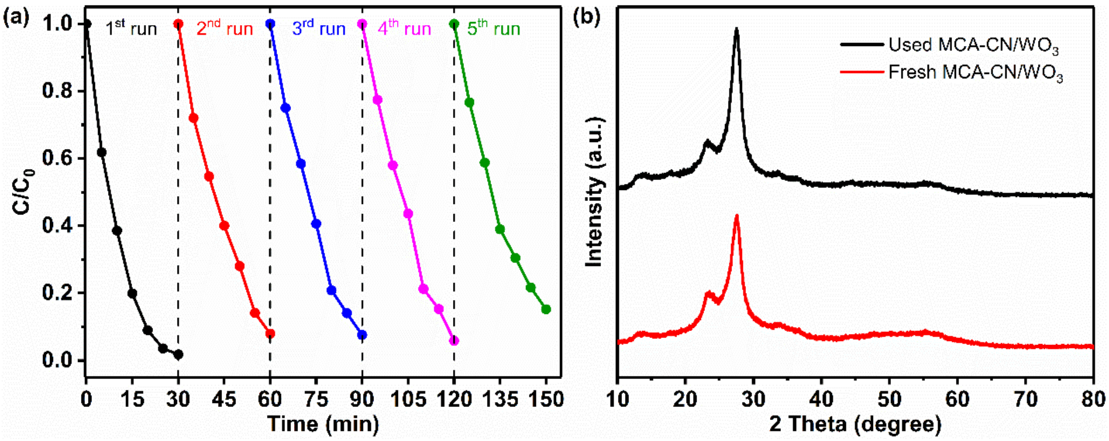

Figure 14. (**a**) Recycling tests of MCA-CN/WO_3 in MB degradation and (**b**) XRD patterns of fresh MCA-CN/WO_3 and used MCA-CN/WO_3.

4. Conclusions

In this study, MCA-CN/WO_3 catalysts were prepared by thermal treatment for MB degradation in photo-Fenton-like processes. The removal efficiency of MB using MCA-CN/WO_3 reached 98% in 30 min, of which the rate constant was about 12.4, 4.7 and 2.1 times higher than that of ME-CN, MCA-CN and ME-CN/WO_3. Such enhanced catalytic performance was mainly attributed to the Z-scheme heterojunction between MCA-CN and WO_3, which accelerated the charge transfer and inhibited the recombination of electrons and holes. In addition, the nanosheet structure and large specific surface area shortened the charge transfer distance and provided abundant active sites, thus improving the catalytic performance of MCA-CN/WO_3. The introduction of WO_3 enhanced the visible light absorption capacity and further promoted the separation of electron–hole pairs. All of these advantages facilitated the decomposition of H_2O_2 to produce $^1O_2$ for the degradation of MB. This study provided a reference to prepare a WO_3-loaded porous carbon nitride nanosheet catalyst for MB degradation in the photo-Fenton-like process.

Supplementary Materials: The following are available online at https://www.mdpi.com/article/10.3390/w14162569/s1, Figure S1. Removal rate of MB by absorption. Figure S2. XRD patterns of MCA-CN/WO_3, 300 °C MCA-CN/WO_3 and 450 °C MCA-CN/WO_3. Figure S3. Different retention time of LC-MS spectrum: (a) 5.75min, (b) 5.13 min, (c) 4.96min, (d) 2.77 min and (e) 2.45 min. Table S1. Summary of the photo-Fenton degradation of pollutants over g-C_3N_4-based photocatalysts. Table S2. Retention time, mass spectra and chemical structure of main degradation intermediates of MB. For more details, please see [5,20,43–46].

Author Contributions: Conceptualization, W.G. and X.Z.; methodology, W.G. and X.Z.; software, W.G.; validation, W.G.; formal analysis, W.G., G.Z., X.Z., S.Z. and Z.W.; investigation, W.G.; resources, W.G.; data curation, W.G.; writing—original draft preparation, W.G.; writing—review and editing, W.G. and X.Z.; visualization, W.G.; supervision, W.G. and X.Z; project administration, X.Z. and S.Z.; funding acquisition, X.Z. All authors have read and agreed to the published version of the manuscript.

Funding: This research was funded by the National Key Research and Development Program of China (Grant No. 2016YFC0400702-2), the National Natural Science Foundation of China (Grant No. 21377041), the Guangdong Science and Technology Program (2020B121201003).

Institutional Review Board Statement: Not applicable.

Informed Consent Statement: Not applicable.

Data Availability Statement: Not applicable.

Conflicts of Interest: The funders had no role in the design of the study; in the collection, analyses, or interpretation of data; in the writing of the manuscript, or in the decision to publish the results.

References

1. Li, X.N.; Ao, Z.M.; Liu, J.Y.; Sun, H.Q.; Rykov, A.I.; Wang, J.H. Topotactic transformation of metal–organic frameworks to graphene-encapsulated transition-metal nitrides as efficient Fenton-like catalysts. *ACS Nano* **2016**, *10*, 11532–11540. https://doi.org/10.1021/acsnano.6b07522.
2. Wols, B.A.; Hofman-Caris, C.H. Review of photochemical reaction constants of organic micropollutants required for UV advanced oxidation processes in water. *Water Res.* **2012**, *46*, 2815–2827. https://doi.org/10.1016/j.watres.2012.03.036.
3. Zhu, J.N.; Zhu, X.Q.; Cheng, F.F.; Li, P.; Wang, F.; Xiao, Y.W.; Xiong, W.W. Preparing copper doped carbon nitride from melamine templated crystalline copper chloride for Fenton-like catalysis. *Appl. Catal. B Environ.* **2019**, *256*, 117830. https://doi.org/10.1016/j.apcatb.2019.117830.
4. Lim, H.; Lee, J.; Jin, S.; Kim, J.; Yoon, J.; Hyeon, T. Highly active heterogeneous Fenton catalyst using iron oxide nanoparticles immobilized in alumina coated mesoporous silica. *Chem. Commun.* **2006**, 4, 463–465. https://doi.org/10.1039/B513517F.
5. Ma, Y.L.; Zhang, J.; Wang, Y.; Chen, Q.; Feng, Z.M.; Sun, T. Concerted catalytic and photocatalytic degradation of organic pollutants over CuS/g-C_3N_4 catalysts under light and dark conditions. *J. Adv. Res.* **2019**, *16*, 135–143. https://doi.org/10.1016/j.jare.2018.10.003.
6. Hu, P.D.; Long, M. Cobalt-catalyzed sulfate radical-based advanced oxidation: A review on heterogeneous catalysts and applications. *Appl. Catal. B Environ.* **2016**, *181*, 103–117. https://doi.org/10.1016/j.apcatb.2015.07.024.
7. Barrio, J.; Lin, L.; Amo-Ochoa, P.; Tzadikov, J.; Peng, G.; Sun, J.; Shalom, M. Unprecedented centimeter-long carbon nitride needles: Synthesis, characterization and applications. *Small* **2018**, *14*, e1800633. https://doi.org/10.1002/smll.201800633.
8. Sun, S.D.; Liang, S.H. Recent advances in functional mesoporous graphitic carbon nitride (mpg-C_3N_4) polymers. *Nanoscale* **2017**, *9*, 10544–10578. https://doi.org/10.1039/C7NR03656F.
9. Xu, R.P.; Li, J.; Sui, G.Z.; Zhuang, Y.; Guo, D.X.; Luo, Z.; Chen, S. Constructing supramolecular self-assembled porous g-C_3N_4 nanosheets containing thiophene-groups for excellent photocatalytic performance under visible light. *Appl. Surf. Sci.* **2022**, *578*, 152064. https://doi.org/10.1016/j.apsusc.2021.152064.
10. Hossein, F.; T.M.-S.; Byeong-Kyu Lee. Efficient photodegradation of Rhodamine B and tetracycline over robust and green g-C_3N_4 nanostructures supramolecular design. *J. Hazard. Mater.* **2021**, *403*, 123703. https://doi.org/10.1016/j.jhazmat.2020.123703.
11. Zhang, K.; Jin, Y.R.; Guo, Y.X.; Wang, H.W.; Liu, K.F.; Fu, W.J.; Wang, B. Study on Microstructure and Photocatalytic Mechanism of g−C_3N_4/WO_3 Heterojunctions Prepared by Ice Template. *Chem. Sel.* **2021**, *6*, 5719–5728. https://doi.org/10.1002/slct.202101168.
12. Meng, J.Q.; Wang, X.Y.; Liu, Y.Q.; Ren, M.; Zhang, X.Y.; Ding. X.H.; Yang, Y. Acid-induced molecule self-assembly synthesis of Z-scheme WO_3/g-C_3N_4 heterojunctions for robust photocatalysis against phenolic pollutants. *Chem. Eng. J.* **2021**, *403*, 126354. https://doi.org/10.1016/j.cej.2020.126354.
13. Li, X.; Song, X.H.; Ma, C.C.; Cheng, Y.M.; Shen, D.; Zhang, S.M.; Wang, H. Direct Z-Scheme WO_3/graphitic carbon nitride nanocomposites for the photoreduction of CO_2. *ACS Appl. Nano Mater.* **2020**, *3*, 1298–1306. https://doi.org /10.1021/acsanm.9b02083.
14. 14. Jun, Y.S.; Lee, E.Z.; Wang, X.; Hong, W.H.; Stucky, G.D.; Thomas, A. From Melamine-Cyanuric acid supramolecular aggregates to carbon nitride hollow spheres. *Adv. Funct. Mater.* **2013**, *23*, 3661–3667. https://doi.org/10.1002/adfm.201203732.
15. Song, T.; Xie, C.; Matras-Postolek, K.; Yang, P. 2D layered g-C_3N_4/WO_3/WS_2 S-Scheme heterojunctions with enhanced photochemical performance. *J. Chem. A* **2021**, *125*, 19382–19393. https:// /doi.org/10.1021/acs.jpcc.1c06753.
16. Bai, X.Y.; Li, Y.; Xie, L.B.; Liu, X.H.; Zhan, S.H.; Hu, W.P. A novel Fe-free photo-electro-Fenton-like system for enhanced ciprofloxacin degradation: Bifunctional Z-scheme WO_3/g-C_3N_4. *Environ. Sci. Nano* **2019**, *6*, 2850–2862. https://doi.org/10.1039/C9EN00528E.
17. Singh, J.; Arora, A.; Basu, S. Synthesis of coral like WO_3/g-C_3N_4 nanocomposites for the removal of hazardous dyes under visible light. *J. Alloy. Compd.* **2019**, *808*, 151734. https://doi.org/10.1016/j.jallcom.2019.151734.
18. Wang, X.; Maeda, K.; Thomas, A.; Takanabe, K.; Xin, G.; Carlsson, J.M.; Antonietti, M. A metal-free polymeric photocatalyst for hydrogen production from water under visible light. *Nat. Mater.* **2009**, *8*, 76–80. https://doi.org/10.1038/NMAT2317.
19. Yang, S.B.; Gong, Y.J.; Zhang, J.L.; Zhan, L.; Ma, L.S.; Fang, Z.Y.; Ajayan, P.M. Exfoliated graphitic carbon nitride nanosheets as efficient catalysts for hydrogen evolution under visible light. *Adv. Mater*. **2013**, *25*, 2452–2456. https://doi.org/10.1002/adma.201204453.
20. Xi, J.H.; Xia, H.; Ning, X.M.; Zhang, Z.; Liu, J.; Mu, Z.J.; Lu, X. Carbon-Intercalated 0D/2D hybrid of hematite quantum dots/graphitic carbon nitride nanosheets as superior catalyst for advanced oxidation. *Small* **2019**, *15*, e1902744. https://doi.org/10.1002/smll.201902744.
21. Liang, Q.H.; Li, Z.; Yu, X.L.; Huang, Z.H.; Kang, F.Y.; Yang, Q.H. Macroscopic 3D porous graphitic carbon nitride monolith for enhanced photocatalytic hydrogen evolution. *Adv. Mater.* **2015**, *27*, 4634–4639. https://doi.org/10.1002/adma.201502057.
22. Zhu, W.Y.; Sun, F.Q.; Goei, R.; Zhou, Y. Construction of WO_3–g-C_3N_4 composites as efficient photocatalysts for pharmaceutical degradation under visible light. *Catal. Sci. Technol.* **2017**, *7*, 2591–2600. https://doi.org/10.1039/C7CY00529F.
23. Ding, J.; Liu, Q.Q.; Zhang, Z.Y.; Liu, X.; Zhao, J.Q.; Cheng, S.B.; Dai, W.L. Carbon nitride nanosheets decorated with WO_3 nanorods: Ultrasonic-assisted facile synthesis and catalytic application in the green manufacture of dialdehydes. *Appl. Catal. B Environ.* **2015**, *165*, 511–518. https://doi.org/10.1016/j.apcatb.2014.10.037.
24. Song, T.; Zhang, X.; Yang, P. Bifunctional nitrogen-doped carbon dots in g-C_3N_4/WO_x heterojunction for enhanced photocatalytic water-splitting performance. *Langmuir* **2021**, *37*, 4236–4247. https://doi.org/10.1021/acs.langmuir.1c00210.

25. Zeng, Y.X.; Liu, C.B.; Wang, L.L.; Zhang, S.Q.; Ding, Y.B.; Xu, Y.Z.; Luo, S. A three-dimensional graphitic carbon nitride belt network for enhanced visible light photocatalytic hydrogen evolution. *J. Mater. Chem.* **2016**, *4*, 19003–19010. https://doi.org/10.1039/C6TA07397B.
26. Liu, D.; Zhang, S.A.; Wang, J.M.; Peng, T.; Li, R.J. Direct Z-Scheme 2D/2D photocatalyst based on ultrathin g-C_3N_4 and WO_3 nanosheets for efficient visible-light-driven H_2 generation. *ACS Appl. Mater. Interfaces* **2019**, *11*, 27913–27923. https://doi.org/10.1021/acsami.9b08329.
27. Li, X.; Kang, B.B.; Dong, F.; Zhang, Z.Q.; Luo, X.D.; Han, L.; Wang, Z.L. Enhanced photocatalytic degradation and H_2/H_2O_2 production performance of S-pCN/$WO_{2.72}$ S-scheme heterojunction with appropriate surface oxygen vacancies. *Nano Energy* **2021**, *81*, 105671. https://doi.org/10.1016/j.nanoen.2020.105671.
28. Wang, J.J.; Wang, Z.Y.; Liu, C.J.J. Enhanced activity for CO oxidation over WO_3 nanolamella supported Pt catalyst. *ACS Appl. Mater. Interfaces* **2014**, *6*, 12860–12867. https://doi.org/10.1021/am502807b.
29. Chen, X.K.; Li, H.; Wu, Y.S.; Wu, H.; Wu, L.F.; Tan, P.; Xiong, X. Facile fabrication of novel porous graphitic carbon nitride/copper sulfide nanocomposites with enhanced visible light driven photocatalytic performance. *J. Colloid. Interf. Sci.* **2016**, *476*, 132–143. https://doi.org/10.1016/j.jcis.2016.05.024.
30. Ahmed, Y.; Yaakob, Z.; Akhtar, P. Degradation and mineralization of methylene blue using a heterogeneous photo-Fenton catalyst under visible and solar light irradiation. *Catal Sci. Technol.* **2016**, *6*, 1222–1232. https://doi.org/10.1039/C5CY01494H.
31. Muruganandham, M.; Swaminathan, M. Photocatalytic decolourisation and degradation of Reactive Orange 4 by TiO-UV process. *Dye. Pigment.* **2006**, *68*, 133–142. https://doi.org/10.1016/j.dyepig.2005.01.004.
32. Yi, Q.Y.; Ji, J.; Shen, B.; Dong, C.C.; Liu, J.; Zhang, J.L.; Xing, M. Singlet oxygen triggered by superoxide radicals in a molybdenum cocatalytic Fenton reaction with enhanced redox activity in the environment. *Environ. Sci. Technol.* **2019**, *53*, 9725–9733. https://doi.org/10.1021/acs.est.9b01676.
33. Zhao, Y.M.; Sun, M.; Wang, X.X.; Wang, C.; Lu, D.W.; Ma, W.; Elimelech, M. Janus electrocatalytic flow-through membrane enables highly selective singlet oxygen production. *Nat. Commun.* **2020**, *11*, 6228. https://doi.org/10.1038/s41467-020-20071-w.
34. Yang, Z.C.; Qian, J.S.; Yu, A.Q.; Pan, B.C. Singlet oxygen mediated iron-based Fenton-like catalysis under nanoconfinement. *Proc. Natl. Acad. Sci. USA* **2019**, *116*, 6659–6664. https://doi.org/10.1073/pnas.1819382116.
35. Pignatello, J.J.; Oliveros, E.; MacKay, A. Advanced oxidation processes for organic contaminant destruction based on the fenton reaction and related chemistry. *Crit. Rev. Environ. Sci. Technol.* **2006**, *36*, 1–84. https://doi.org/10.1080/10643380500326564.
36. Laura, A. MacManus-Spencer, K.M. Quantification of singlet oxygen production in the reaction of superoxide with hydrogen peroxide using a selective chemiluminescent. *Probe* **2005**, *127*, 8954–8955. https://doi.org/10.1021/ja052045b.
37. Zheng, N.C.; He, X.; Hu, R.T.; Wang, R.L.; Zhou, Q.; Lian, Y.K.; Hu, Z. In-situ production of singlet oxygen by dioxygen activation on iron phosphide for advanced oxidation processes. *Appl. Catal. B Environ.* **2022**, *307*, 121157. https://doi.org/10.1016/j.apcatb.2022.121157.
38. Jia, J.K.; Jiang, C.Y.; Zhang, X.R.; Li, P.J.; Xiong, J.X.; Zhang, Z.Z.; Wang, Y. Urea-modified carbon quantum dots as electron mediator decorated g-C_3N_4/WO_3 with enhanced visible-light photocatalytic activity and mechanism insight. *Appl. Surf. Sci*. **2019**, *495*, 143524. https://doi.org/10.1016/j.apsusc.2019.07.266.
39. Jain, B.; Singh, A.K.; Kim, H.; Lichtfouse, E.; Sharma, V.K. Treatment of organic pollutants by homogeneous and heterogeneous Fenton reaction processes. *Environ. Chem. Lett.* **2018**, *16*, 947–967. https://doi.org/10.1007/s10311-018-0738-3.
40. Zhao, H.Y.; Chen, Y.; Peng, Q.S.; Wang, Q.N.; Zhao, G.H. Catalytic activity of MOF(2Fe/Co)/carbon aerogel for improving H_2O_2 and OH generation in solar photo–electro–Fenton process. *Appl. Catal. B Environ.* **2017**, *203*, 127–137. https://doi.org/10.1016/j.apcatb.2016.09.074.
41. Yin, Y.; Ren, Y.; Lu, J.H.; Zhang, W.M.; Shan, C.; Hua, M.; Pan, B. The nature and catalytic reactivity of UiO-66 supported Fe_3O_4 nanoparticles provide new insights into Fe-Zr dual active centers in Fenton-like reactions. *Appl. Catal. B Environ.* **2021**, *286*, 119943. https://doi.org/10.1016/j.apcatb.2021.119943.
42. Zhou, S.Q.; Wang, Y.; Zhou, K.; Ba, D.Y.; Ao, Y.H.; Wang, P.F. In-situ construction of Z-scheme g-C_3N_4/WO_3 composite with enhanced visible-light responsive performance for nitenpyram degradation. *Chin. Chem. Lett.* **2021**, *32*, 2179–2182. https://doi.org/10.1016/j.cclet.2020.12.002.
43. Wang, L.; Zhu, Y.; Yang, D.; Zhao, L.; Ding, H.; Wang, Z. The mixed marriage of copper and carbon ring-g-C3N4 nanosheet: A visible-light-driven heterogeneous Fenton-like catalyst. *Appl. Surf. Sci.* **2019**,*488*, 728–738, https://doi.org/10.1016/j.apsusc.2019.05.288.
44. Zhang, J., Zhang, G., Ji, Q.H., Lan, H.C., Qu, J.H., Liu, H.J. Carbon nanodot-modified FeOCl for photo-assisted Fenton reaction featuring synergistic in-situ H_2O_2 production and activation. *Appl. Catal. B.* **2020**, 266, 118665. https://doi.org/10.1016/j.apcatb.2020.118665.
45. An, S.F., Zhang, G.H., Wang, T.W., Zhang, W.N., Li, K., Song, C.S.nHigh-Density Ultra-small Clusters and Single-Atom Fe Sites Embedded in Graphitic Carbon Nitride (g-C_3N_4) for Highly Efficient Catalytic Advanced Oxidation Processes. *ACS Nano.* **2018**, 12, 9441–9450. https://doi.org/10.1021/acsnano.8b04693.
46. Li, X., Pi, Y.H., Wu, L.Q., Xia, Q.B., Wu, J.L., Li, Z. Facilitation of the visible light-induced Fenton-like excitation of H_2O_2 via heterojunction of g-C_3N_4/NH_2-Iron terephthalate metal-organic framework for MB degradation. *Appl. Catal. B*. **2017**, 202, 653-663. https://doi.org/10.1016/j.apcatb.2016.09.073